Nanoscale

Dynamics of Ionic Liquids in the Presence of Polymer-Grafted Nanoparticles

Journal:	*Nanoscale*
Manuscript ID	NR-ART-05-2019-004204.R1
Article Type:	Paper
Date Submitted by the Author:	12-Jul-2019
Complete List of Authors:	Liu, Siqi; Stevens Institute of Technology, Chemical Engineering & Materials Science Liedel, Clemens; Max-Planck Institute of Colloids and Interfaces, Department of Colloid Chemistry Tarakina, Nadezda; Max-Planck-Institut fur Kolloid und Grenzflachenforschung, Colloid Chemistry Osti, Naresh; Clemson University, Akcora, Pinar; Stevens Institute of Technology, Chemical Engineering & Materials Science

Dynamics of Ionic Liquids in the Presence of Polymer-Grafted Nanoparticles

Siqi Liu[†], *Clemens Liedel*[§], *Nadezda V. Tarakina*[§], *Naresh C. Osti*[¶] *and Pinar Akcora**[,†]

[†]Department of Chemical Engineering & Materials Science, Stevens Institute of Technology

Hoboken, NJ 07030, USA

[§]Department of Colloid Chemistry, Max Planck Institute of Colloids and Interfaces

Research Campus Golm, Potsdam 14476, Germany

[¶]Neutron Scattering Division, Oak Ridge National Laboratory

Oak Ridge, Tennessee 37831, USA

*Corresponding Author. Email: pakcora@stevens.edu

KEYWORDS: polymer-grafted nanoparticles, ionic liquid, zwitterionic liquid, solvation, dynamic coupling, quasi-elastic neutron scattering, translational diffusion.

Abstract

We incorporated polymer-grafted nanoparticles into ionic and zwitterionic liquids to explore the solvation and confinement effects on their heterogeneous dynamics using quasi-elastic neutron scattering (QENS). 1-hexyl-3-methylimidazolium bis(trifluoromethylsulfonyl)imide (HMIM-TFSI) mixed with deuterated poly(methyl methacrylate) (d-PMMA)-grafted nanoparticles is studied to unravel how dynamic coupling between PMMA and HMIM-TFSI influence the fast and slow diffusion characteristics of the $HMIM^+$ cations. The zwitterionic liquid, 1-butyl-3-methyl imidazole-2-ylidene borane (BMIM-BH_3) is critically selected and mixed with PMMA-grafted nanoparticles for comparison in this work as its ions do not self-dissociate and it does not couple with PMMA through ion-dipole interactions as HMIM-TFSI does. We find that long-range unrestricted diffusion of $HMIM^+$ cations is higher in well-dispersed particles than in aggregated particle systems, whereas the localized diffusion of $HMIM^+$ is measured to be higher in close-packed particles. Translational diffusion dynamics of BMIM-BH_3 is not influenced by any particle structures suggesting that zwitterions do not interact with PMMA. This difference between two ionic liquid types enables us to decouple polymer effects from the diffusion of ionic liquids, which is integral to understand the ionic transport mechanism in ionic liquids confined in polymer-grafted nanoparticle electrolytes.

1. Introduction

Ionic liquids (ILs) are molten salts that have melting temperatures lower than 100 ^oC. They exhibit outstanding advantages over other solvents, such as negligible vapor pressure, high thermal and electrochemical stability. These properties make ILs designer liquids for various applications in electrochemical energy storage systems[1-3], gas capturing, or membrane separation processes[4-6]. ILs usually consist of inorganic anions and asymmetric organic cations which contain polar heads and alkyl chains. The structural and dynamical heterogeneities of ILs were investigated in both simulations[7-9] and experiments using neutron spin echo spectroscopy[10], X-ray diffraction[8, 11], and quasi-elastic neutron

spectroscopy[12, 13]. Both heterogeneities were affected by the confinement of IL inside different hosts (e.g. porous structures) where fastening[14, 15] or slowing down[16-18] in translational motion of IL was measured. Surface chemistry, size and charging state of the pores influence the dynamics of electrolyte ions through the rearrangement of molecules within IL aggregates[19]. It was recently suggested that the molecular conformation of IL ions is altered upon applying electric fields when they are confined in mesoporous carbon[20]. Mobility of ions and controlling ionic aggregation in bulk ILs leads to their high ionic conductivity. For example, adding aprotic solvents to IL screens anion-cation interactions and hence solvates the ion clusters[21].

Polymers solvated by imidazolium salts exhibit better thermal stability and lower glass-transition temperature[22-24]. It was shown that Coulombic interactions between poly(methyl methacrylate) (PMMA) and $TFSI^-$ anion of 1-ethyl-3-methylimidazolium bis(trifluoromethylsulfonyl)imide (EMIM-TFSI) can prohibit the formation of ion clusters[24]. The ion-dipole interactions between $TFSI^-$ and PMMA can self-dissociate the EMIM-TFSI, thereby increase the number of free cation carriers. Two relaxations of the $EMIM^+$ measured in quasi-elastic neutron scattering spectrometer were attributed to the dynamics of free ions in bulk EMIM-TFSI and to the ions that were bound to the PMMA[12]. The slower dynamic process was assigned to the higher T_g of IL when it bounded with PMMA; and the faster dynamics was for the bulk IL. Motion of ions coupled to the polymer was found to be slower than the translational diffusion of free ions[12]. These findings on PMMA-based ion gels are critically important for designing soft and mechanically strong membranes with high ionic conductivity and thermal stability for their applications in electrochemical devices.

In this study, dynamics of $HMIM^+$ cations of 1-hexyl-3-methylimidazolium bis(trifluormethylsulfonyl)imide (HMIM-TFSI) containing PMMA-grafted Fe_3O_4 nanoparticles is investigated in quasi-elastic neutron scattering (QENS). Using deuterated grafted chains, we were able to selectively probe the diffusion of $HMIM^+$ cations. This local dynamics information is then coupled to the dispersion of PMMA-grafted nanoparticles in HMIM-TFSI, and the effects of solvation, Coulombic interactions and spatial confinement of HMIM-TFSI within particle structures are discussed. The IL-

particles system is compared with a particle-free system to assess how the cation diffusion is influenced by the PMMA-grafted particles. Furthermore, comparison of QENS results on the dynamics of $HMIM^+$ cations within well-dispersed and aggregated grafted particle structures allows us to gain an insight on the influence of ion-polymer interactions on the ion transport mechanism. To complement and achieve this important task, a new zwitterionic liquid (ZIL)[25], 1-butyl-3-methyl imidazole-2-ylidene borane (BMIM-BH_3) is utilized as a solvating medium for the PMMA-grafted particles. Because of the zwitterionic nature, ions do not self-dissociate in this new ZIL, hence ionic motions are expected to decouple from interactions between PMMA and ionic liquid. Thus, it is anticipated that the QENS signals from particles in BMIM-BH_3 result from more simple relaxation processes where BMIM-BH_3 freely diffuses without interacting with polymers. This feature will enable decoupled ion transport in polymer electrolytes, which is not possible with the current self-associating ILs.

2. Experimental Section

Sample Preparation. Deuterated MMA (d8-MMA 98%) and 1-hexyl-3-methylimidazolium bis(trifluoromethylsulfonyl)imide (HMIM-TFSI) were purchased from Polymer Source and IoLitec, Ionic Liquids Technologies, respectively. The zwitterionic liquid 1-butyl-3-metylimidazol-2-ylidene borane (BMIM-BH_3), shown in Scheme 1, was prepared as described previously[25]. This new IL has good solubility in toluene, low viscosity of 181 cP at 25 °C, and it is thermally stable at 100 °C. Its electrochemical reductive stability is better than similar conventional ILs and its simple one-pot synthesis offers its use in electrochemical devices[25, 26]. 4-cyanopentanoic acid dithiobenzoate (CPDB), diethyl ether, oleic acid (90%) and oleylamine (70% technical grade) were purchased from Sigma-Aldrich. Tetrahydrofuran (THF) and cyclohexane (both ACS grades) were purchased from Pharmco-AAPER. 2,2'-Azobis(isobutyronitrile) (AIBN; 98% technical grade) was recrystallized from methanol. All other chemicals were used as received.

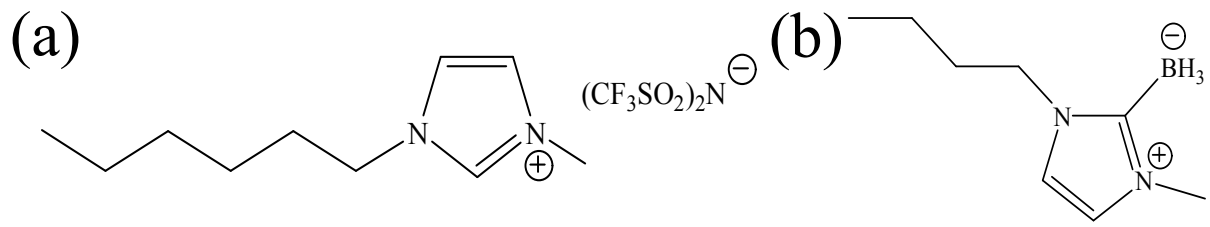

Scheme 1. Structure of **(a)** HMIM-TFSI and **(b)** zwitterionic liquid, BMIM-BH_3.

Nanoparticle Synthesis. Fe_3O_4 nanoparticles of 26 nm and 7 nm in diameter were synthesized by high-temperature thermal decomposition method. The synthetic procedure of nanoparticles (26±3 nm) capped with oleic acid includes two steps[27]: synthesis of iron-oleate complex by ion exchange of iron chloride and sodium oleate salts; and thermal decomposition of the iron-oleate precursor. The one-step reaction of (7±1 nm) nanoparticles utilizes iron(III)acetylacetonate, $Fe(acac)_3$, as a precursor and uses both oleic acid and oleylamine as surface ligands[28] which results in nanoparticles at high yields with no by-products. Particle size and distributions were obtained by analyzing the transmission electron microscopy (TEM) data in ImageJ through sampling over hundreds of particles. The representative TEM micrographs of bare particles and their particle size histograms are shown in Fig. S1†.

Preparation of CPDB-Anchored Fe_3O_4 Nanoparticles. CPDB (4 mg/mL in THF) was added drop-wise into nanoparticle solution of 2 mg/mL and sonicated in a bath sonicator. The mixture was stirred at room temperature for 24 h. Particles were washed following the previously reported protocol to remove excess CPDB[29]. The mixture was precipitated by adding a large amount of cyclohexane and ethyl ether (4:1 volume ratio), centrifuged at 3,000 rpm for 15 min and re-dissolved in 25 mL of THF. The washing procedure was repeated three times.

Surface-Initiated Reversible Addition-Fragmentation Chain-Transfer (SI-RAFT) Polymerization of d-MMA on Fe_3O_4 Nanoparticles. CPDB-anchored Fe_3O_4 particles, d-MMA and AIBN in THF solution were degassed in freeze-pump-thaw cycles. The flask was placed in an oil bath and stirred at 60 ^oC for 6 h. The flask was immersed in ice water to terminate the polymerization via quenching. To purify the grafted particles, ethanol was added to the solution and centrifuged at 6,000 rpm. The washing step

was repeated several times till the supernatant solution was clear after addition of ethanol. The supernatant was removed, and particles were re-dissolved in THF. This procedure was repeated several times to remove the free PMMA chains.

Structural Characterization. TEM data were collected using two instruments, FEI TITAN THEMIS 200 TEM located at the CUNY-ASRC Imaging Facility operated at 200 kV and a double Cs corrected JEOL JEM-ARM200F (S)TEM operated at 80 kV and equipped with a cold-field emission gun and a high-angle silicon drift Energy Dispersive X-ray (EDX) detector (solid angle up to 0.98 steradians with a detection area of 100 mm^2) at the Max Planck Institute of Colloids and Interfaces, Germany. Annular dark field scanning transmission electron microscopy (ADF - STEM) images were collected at a probe convergence semi-angle of 15 mrad. PMMA-grafted particles in ionic liquid solution were drop cast on lacey carbon grids. Samples for TEM are at lower particle concentrations compared to the samples for QENS.

Weight losses of polymer-grafted particles were measured in thermo-gravimetric analyzer (Q50 TGA, TA Instruments), and the grafting densities were calculated as reported in the previous work[30]. The weight-averaged molecular weight (M_w) of d-PMMA grafted on 26 nm particles was determined using a gel permeation chromatography-light scattering (GPC/LS) device after etching the particles. The GPC/LS system in our laboratory is equipped with a VARIAN PL 5.0μm Mixed–C gel column (7.5 mm ID), a light scattering detector (miniDawn, Wyatt Technology) and a refractive index detector (Optilab rEX, Wyatt).

The molecular weight of d-PMMA grafted chains on 7 nm particles was estimated by utilizing our TGA data library of synthesized grafted particles collected over the years in our laboratory. The mass ratio of grafted chains and core particles (m_{PMMA}/m_{NP}) was plotted as a function of the ratio of grafting density (σ) and M_w by compiling the data of particles with graft densities lower than 0.2 chains/nm^2 (shown in Fig. S2†). With the measured mass ratios of samples, the corresponding grafting densities and molecular weights for these two samples were determined by using the calibration line of the weight loss amounts for varying (σ/M_w). Particles grafted on 26 nm particles were measured to have 138.4 kDa

(dispersity of 1.05) d-PMMA chains at 0.09 chains/nm^2 density as determined by GPC/LS and TGA instruments. Samples measured in QENS experiments are summarized in Table 1. Note that 138.4 kDa sample has a larger particle core size.

Table 1. Characteristics of d-PMMA-grafted Fe_3O_4 nanoparticles.

grafted chain M_w (kDa)	grafting density, σ (chains/nm^2)	particle core size (nm)
39.9	0.08	7±1
40.2	0.11	7±1
138.4	0.09	26±3

Quasi-Elastic Neutron Scattering (QENS). QENS experiments were performed on the BASIS backscattering spectrometer at the Spallation Neutron Source, Oak Ridge National Laboratory[31]. The final energy of scattered neutrons was selected by Si(111) analyzer crystals with a Bragg reflection at 88^o and a wavelength of λ = 6.27 Å, providing energy resolution of 3.5 μeV and momentum transfer vector (Q) range of 0.2-2.0 Å^{-1}. The dynamic range was chosen as ±100 μeV for data analysis. Grafted particles were mixed with HMIM-TFSI or BMIM-BH_3 at 2.5-3.5 wt% particle concentrations. 0.5 mL sample solution was loaded into cylindrical annular aluminum sample holders of 0.05 mm gap. Sample cans were sealed with 0.06 mm indium O-ring. Sample temperature was controlled using a closed cycle refrigerator (CCR). First, we performed elastic scans at 300 K on each sample of grafted particle solutions. Samples were then cooled down to 20 K to measure the sample specific instrument resolution. Elastic intensity data was recorded by ramping up the temperature from 20 K to 375 K at a heating rate of 5 K/min. Data at 300 K of neat HMIM-TFSI and BMIM-BH_3 was collected during heating from 20 K to 375 K. QENS spectra were collected at 300 K and 340 K for the neat liquids and at 300 K for the grafted samples. Data was reduced by the Mantid software[32] and was analyzed using the DAVE software[33].

3. Results and Discussion

Elastic and quasi-elastic neutron scattering results of two model ionic liquids, HMIM-TFSI and BMIM-BH_3, in the presence of polymer-grafted nanoparticles are investigated to understand how particle structures and polymer coupling influence dynamic processes of ions.

Elastic neutron scattering. The elastic intensity at zero energy transfer was measured in fixed energy window scans as a function of temperature. Elastic intensity decreases sharply at the temperature where dynamic processes are activated which are fast enough to enter the spectrometer resolution window[34, 35]. The monotonic decrease of elastic intensities averaged over Q=0.2-2.0 $Å^{-1}$ during heating is shown in Fig. 1. The data of two PMMA-grafted particles (39.9 kDa d-PMMA with 0.08 chains/nm^2 graft density and 40.2 kDa d-PMMA with 0.11 chains/nm^2 graft density) overlaps with the elastic intensity data of their corresponding neat ionic liquids. Fig. 1a and c show the elastic intensities of these two grafted particles in BMIM-BH_3 and in HMIM-TFSI, respectively. The sharp increase in the elastic intensity at around 250 K is designated to the crystallization of HMIM-TFSI, which is in agreement with differential scanning calorimetry (DSC) measurement that shows an exothermal peak due to crystallization of the low temperature amorphous phase at 250 K (Fig. S3†). This elastic behavior is similar to the crystallization observed in other type of ionic liquids[35]. The crystallization temperature of neat HMIM-TFSI was reported as 243 K in a previous work[36]. The mean-squared displacement, $\langle u^2 \rangle$, can be extracted by fitting the elastic intensity with the equation[12]: $I(Q, E = 0) \propto \exp\left(-\frac{1}{3}\langle u^2 \rangle Q^2\right)$ and starts to diverge around the glass-transition temperature (T_g) of each ionic liquid. T_g's of 252 K and 229 K, which are higher than T_g's measured in DSC ($T_{g,\ BMIM\text{-}BH3}$: 208 K[25] and $T_{g,\ HMIM\text{-}TFSI}$: 183 K[37]), are marked in Fig 1 for neat BMIM-BH_3 and HMIM-TFSI, respectively. With the addition of PMMA-grafted particles to each ionic liquids, T_g's are unchanged.

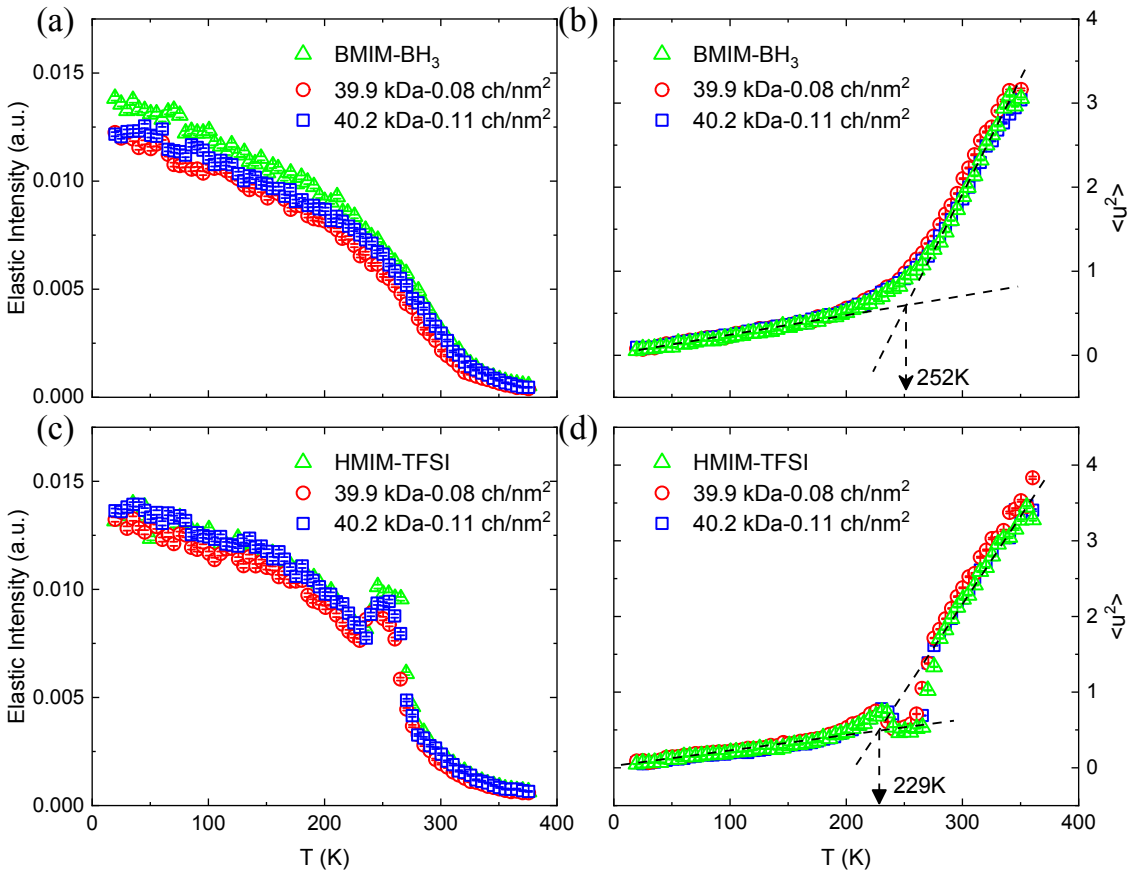

Fig. 1 Q-averaged elastic intensities and mean-squared displacements of the neat and d-PMMA-grafted nanoparticles in **(a-b)** $BMIM\text{-}BH_3$ and in **(c-d)** HMIM-TFSI as a function of temperature. T_g is marked on the mean-squared displacements plots with an arrow.

Dynamic processes measured in QENS. QENS is a powerful technique to measure the dynamic processes on the time scale of a few picoseconds and length scale below one nanometer. Dynamic characteristics such as jump diffusion coefficient (D), characteristic residence time between jumps (τ) and jump length (l) can be obtained from quasi-elastic scattering. QENS is sensitive to isotopes with large incoherent neutron scattering cross sections. The incoherent scattering, coherent scattering and absorption cross sections of all species used in this work are given in Table S1. As shown, the incoherent scattering cross sections of Fe_3O_4 and d-PMMA are completely negligible. The scattering signal mostly comes from the protons of $HMIM^+$ and of $BMIM\text{-}BH_3$. QENS spectra were collected above the melting temperature of each ionic liquid. The normalized QENS spectra of two sets of samples (PMMA-grafted particles in

HMIM-TFSI and BMIM-BH_3) at Q = 1.5 $Å^{-1}$ are presented in Figs. 2a-b. We analyzed the dynamic structure factor with a sum of two Lorentzian functions using the DAVE software. The measured QENS intensity as a function of energy at specific Q is given by the following equation and shown in Fig. 2a-b:

$I(Q,E) = [X_1(Q)\delta(E) + (1 - X_1(Q))S(Q,E)] \otimes R(Q,E) + B(Q,E)$, where $X_1(Q)$ represents the fraction of elastic scattering, δ(E) is the delta function, S(Q,E) is the dynamic structure factor, B(Q,E) is the linear background term, R(Q,E) is the instrument resolution function. S(Q,E) of pure ionic liquid and grafted particles in ionic liquids were fit with a sum of two Lorentzian functions[1, 14] for two different processes of slow and fast dynamics: $S(Q,E) = p_2(Q)\frac{1}{\pi}\frac{\Gamma_1(Q)}{\Gamma_1(Q)^2 + E^2} + (1 - p_2(Q))\frac{1}{\pi}\frac{\Gamma_2(Q)}{\Gamma_2(Q)^2 + E^2}$, where $p_2(Q)$ and $(1\text{-}p_2(Q))$ are relative weight of the second and first Lorentzians. $\Gamma_1(Q)$ and $\Gamma_2(Q)$ terms represent the broadenings in the S(Q, E) functions in terms of half widths at half maxima (HWHM) of double Lorentzian functions for the fast and slow dynamic components, respectively.

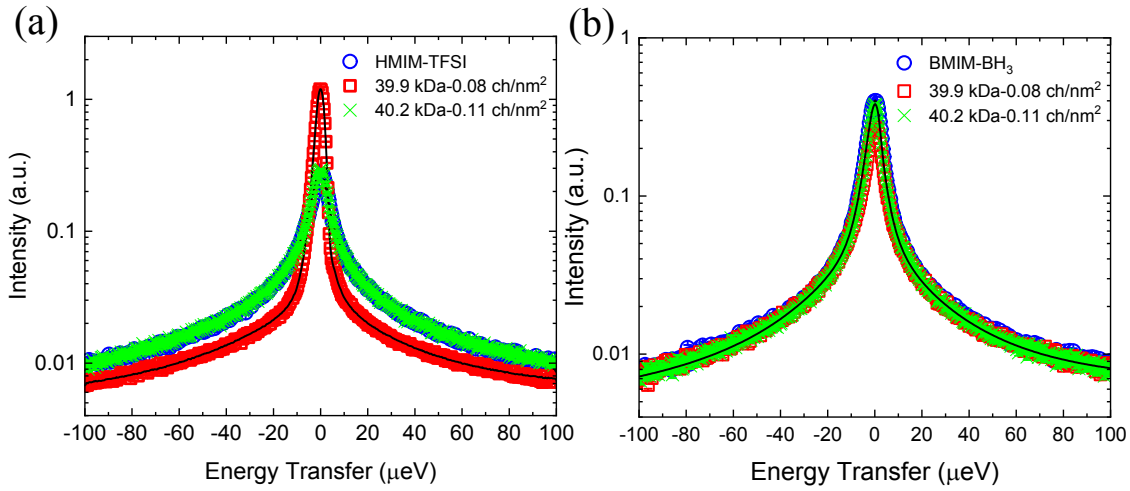

Fig. 2 Representative QENS spectra of **(a)** pure HMIM and HMIM with PMMA-grafted particles, **(b)** pure BMIM-BH_3 and BMIM-BH_3 with PMMA-grafted particles at 300 K, Q = 1.5 $Å^{-1}$. The black solid lines are the total fitting to the scattering data.

The two-component model was used to describe the translational dynamic processes of neat IL[35, 38, 39] and IL that is confined in ionogels[16] and in nanopores[1]. In classic translational diffusion, the HWHM has a Q^2-dependence which is described by the jump dynamics model, as expressed by the equation: $\Gamma(Q) =$

$\frac{\hbar DQ^2}{1+DQ^2\tau}$. D is the diffusion coefficient, τ is the characteristic time between jumps of a diffusive entity (residence time) and ℏ is the reduced Planck's constant. The HWHM of the Lorentzian QENS broadening of pure HMIM and BMIM-BH_3 at 300 K and 340 K are shown in Fig. 3. The broad and narrow Lorentzian broadenings fit to a jump diffusion model, representing the translational motions. The broad component is related to local constrained translational diffusion for the faster process (Fig. 3a). The narrow component is associated with long-range unrestricted translational diffusion for the slower process (Fig. 3b). Diffusion coefficients obtained from the fast and slow dynamics processes for two temperatures are shown in Table 2. The local translational diffusion (D_{fast}) and the long-range diffusion coefficients (D_{slow}) are very close for both HMIM and BMIM-BH_3 at 300 K. D_{fast} (local translational dynamics) slightly decreases as temperature increases to 340 K. D_{slow} increases at 340 K for both HMIM and BMIM-BH_3. We note that for slow motion at 340 K, the model fits well to the experimental data between 0.3−1.3 $Å^{-1}$ Q range (Fig. 3b). The drop in data points at Q = 1.7 $Å^{-1}$ for both pure HMIM and pure BMIM-BH_3 at 340 K indicates the narrowing of quasi-elastic line width which is a result of the molecular confinement as defined by the de Gennes narrowing effect[40]. Note that HWHM levels off for the fast component below 0.9 $Å^{-1}$ for pure BMIM-BH_3 and 0.5 $Å^{-1}$ in pure HMIM-TFSI (Fig. 3a) indicating the spatially confined dynamics within ionic clusters in pure ionic liquids. The radius of a sphere (a) where particles are confined can be calculated by fitting the elastic incoherent structure factor (EISF) to the Equation[35, 38, 41]: $\mathrm{EISF} = c_1 + (1 - c_1)\left(\frac{3j_1(Qa)}{Qa}\right)^2$, where j_1 is the first order of spherical Bessel function and c_1 is the "immobile fraction". The EISF graphs are presented in Fig. S4†. The confinement radius (a) is found to be 3.67±0.28 Å for BMIM-BH_3 and 4.05±0.24 Å for HMIM-TFSI. c_1 is calculated as 0.08 and 0.05 for BMIM-BH_3 and HMIM-TFSI, respectively. These results are reasonable as ionic aggregation will be limited in BMIM-BH_3 because of its zwitterionic character. In addition, we calculated fractions of fast and slow diffusion processes using the areas of two Lorentzian functions for pure HMIM-TFSI and pure BMIM-BH_3 (Fig. 4). Fraction of the protons participating in the fast process (local constrained translational motion) increases with increasing Q at 340 K more than that measured at 300 K. At high Q,

it reaches to 0.8 at 340 K for both liquids. These results combined with EISF analysis result support the spatially confined process of local dynamics. Our result is consistent with the QENS results of dIM-TFSI as reported by Hoarforst et al[42].

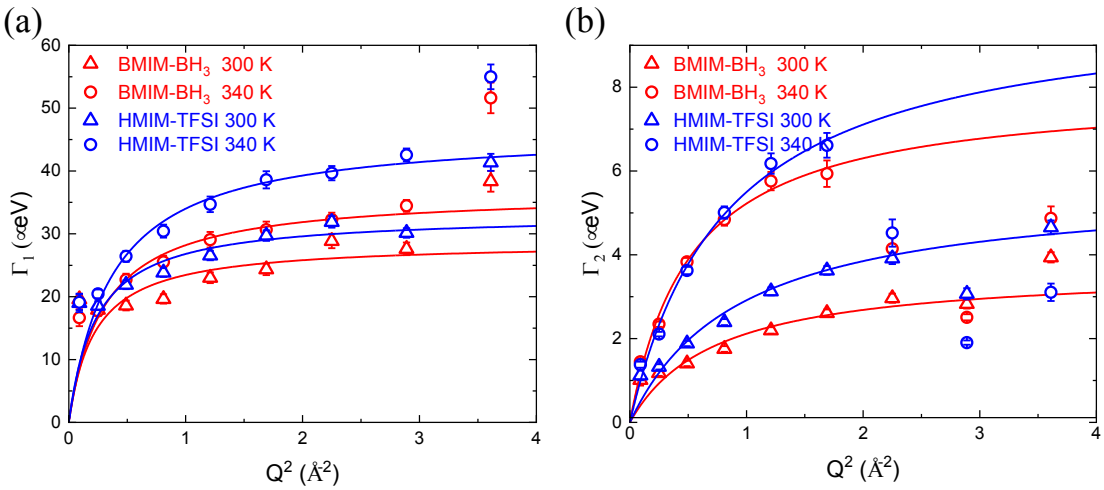

Fig. 3 Quadratic dependence of HWHM from double Lorentzian broadenings of pure HMIM-TFSI and pure BMIM-BH_3 for **(a)** fast and **(b)** slow processes. Lines show the jump diffusion model fits to the data. Error bars represent the standard deviation of the Lorentzian fits.

Table 2. Diffusion coefficients (D) of neat HMIM-TFSI and BMIM-BH_3 for fast and slow processes.

	neat HMIM-TFSI		neat BMIM-BH_3	
Temperature (K)	D_{fast} (10^{-10} m^2 s^{-1})	D_{slow} (10^{-10} m^2 s^{-1})	D_{fast} (10^{-10} m^2 s^{-1})	D_{slow} (10^{-10} m^2 s^{-1})
300	21.46±3.99	0.91±0.15	19.56±6.66	0.76±0.13
340	19.24±1.93	1.84±0.24	18.61±1.85	2.31±0.28

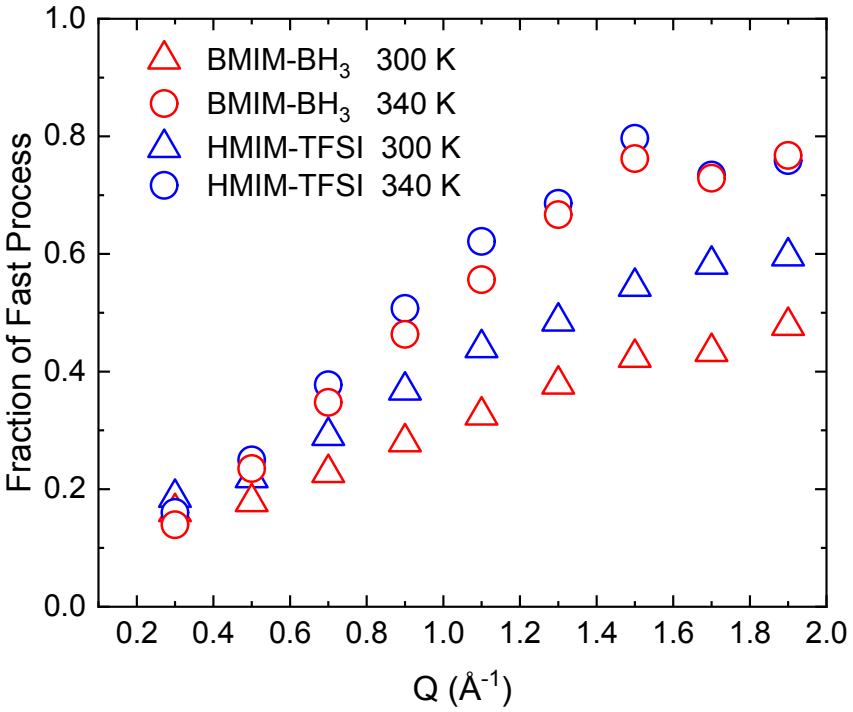

Fig. 4 Fraction of fast process as a function of Q at 300 K and 340 K of neat HMIM-TFSI and neat BMIM-BH_3.

Next, we discuss the most prominent result of the study, which is the interpretation of QENS data of HMIM-TFSI and BMIM-BH_3 in the presence of d-PMMA-grafted nanoparticles. Akin to data analysis of pure ionic liquids, slow and fast process dynamics are analyzed by applying the jump diffusion model (Fig. 5). The effective fast and slow diffusion coefficients obtained from the model fits are listed in Table S2a-b. Characteristic residence times and jump distances are given in Tables S3-S4, respectively. The lowest Q value is excluded from the fittings in fast processes for BMIM-BH_3 and HMIM-TFSI (Fig. 5a and 5b).

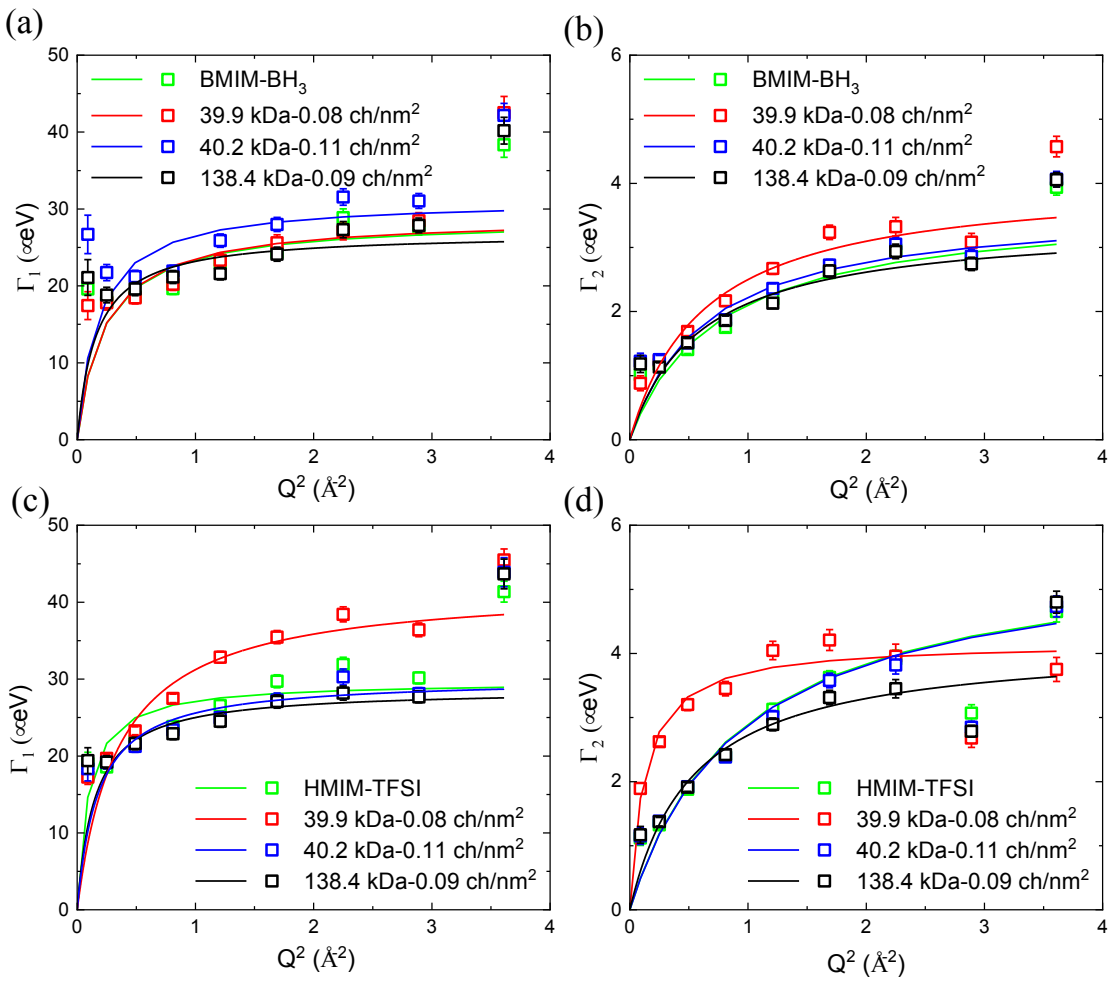

Fig. 5 Quadratic dependence of HWHM from double Lorentzian functions fit to QENS signals of PMMA-grafted nanoparticles in **(a-b)** BMIM-BH_3 and in **(c-d)** HMIM-TFSI. (a, c) are the fast and (b, d) are the slow components. Lines show the jump diffusion model fits to the HWHM extracted from the QENS data. Note that Q values of 0.3 $Å^{-1}$ and 1.9 $Å^{-1}$ are excluded from the fitting for all solutions in the fast processes. For the slow process, data at Q values of 1.7 $Å^{-1}$ is excluded for all HMIM-TFSI solutions; and Q values of 0.3 $Å^{-1}$ and 1.9 $Å^{-1}$ are excluded in all BMIM-BH_3 solutions. In 138.4 kDa-grafted particles sample, data points at 0.3 $Å^{-1}$ and 1.9 $Å^{-1}$ are excluded from the fitting.

Fig. 6 shows the long-range dynamic processes (D_{slow}) and the localized diffusion processes (D_{fast}) from the confined regions of $HMIM^+$ and BMIM-BH_3 with the d-PMMA-grafted particles. With the short

grafted chains (39.9 kDa), D_{slow} of $HMIM^+$ is observed to be higher by a factor of 5 (5.03 x 10^{-10} m^2/s) compared to the other two grafted particles (approx. 1 x 10^{-10} m^2/s) and neat HMIM-TFSI (0.91 x 10^{-10} m^2/s). We attribute the enhanced diffusivity of $HMIM^+$ to the increased number of free cations as a result of $TFSI^-$ coupling with PMMA in the well-dispersed particles at the low grafting density (39.9 kDa, 0.08 chains/nm^2, Fig. 7a). D_{fast}, which denotes the locally constrained motions of cations, is the highest (58.04 x 10^{-10} m^2/s, by a factor of 3 compared to the neat IL) in the sample with close-packed particle monolayer (40.2 kDa with 0.11 chains/nm^2, Fig. 7b) as $HMIM^+$ dynamics can be accelerated due to its confinement in this observed structure. Weak penetration of HMIM-TFSI into 138.4 kDa grafted particles with 0.09 chains/nm^2 presumably lead to the phase separation of grafted particles as seen in Fig. 7c, hence D_{slow} and D_{fast} of $HMIM^+$ are found to be very close to that in neat form (0.91 x 10^{-10} m^2/s and 21.46 x 10^{-10} m^2/s, respectively). Furthermore, EDX analysis on PMMA-grafted particles confirm that ionic liquids solvate the chains around the particles (Fig. 8a). The sulfur group in the end-group of PMMA chains is verified with data presented in Fig. 8b. To the best of our knowledge, this is the first time grafted chains are observed under scanning transmission electron microscope at this resolution. EDX elemental maps at a lower magnification show where the ionic liquids are located on the grids. As seen in Fig. S5a-b†, there is no phase separation between HMIM-TFSI and particles, indicating good miscibility between grafted PMMA chains and ionic liquids at large scale. The boron in BMIM-BH_3 is distributed uniformly over particles as well (Fig. S5c†).

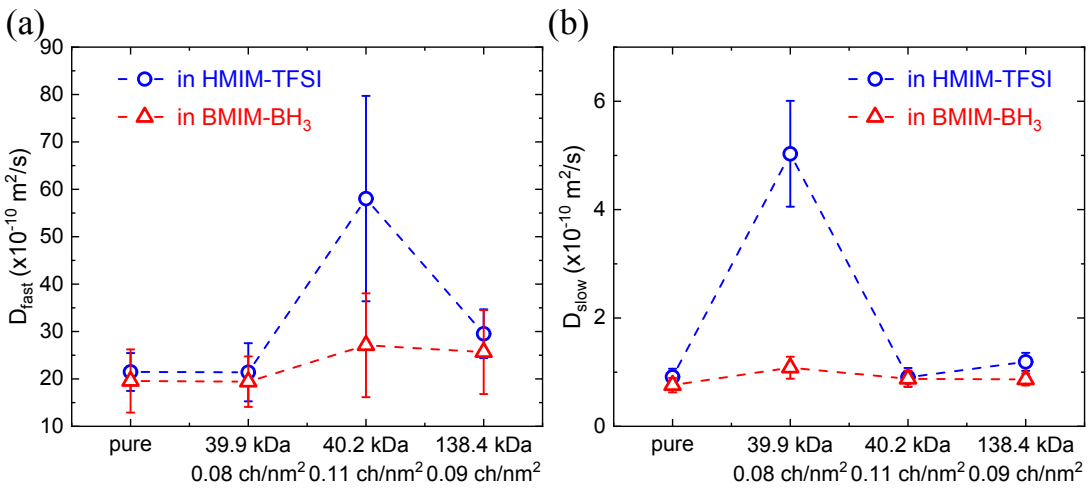

Fig. 6 (a) Local diffusivities (D_{fast}) and **(b)** long-range translational diffusivities (D_{slow}) of $HMIM^+$ and BMIM-BH_3 with three different PMMA grafted nanoparticles.

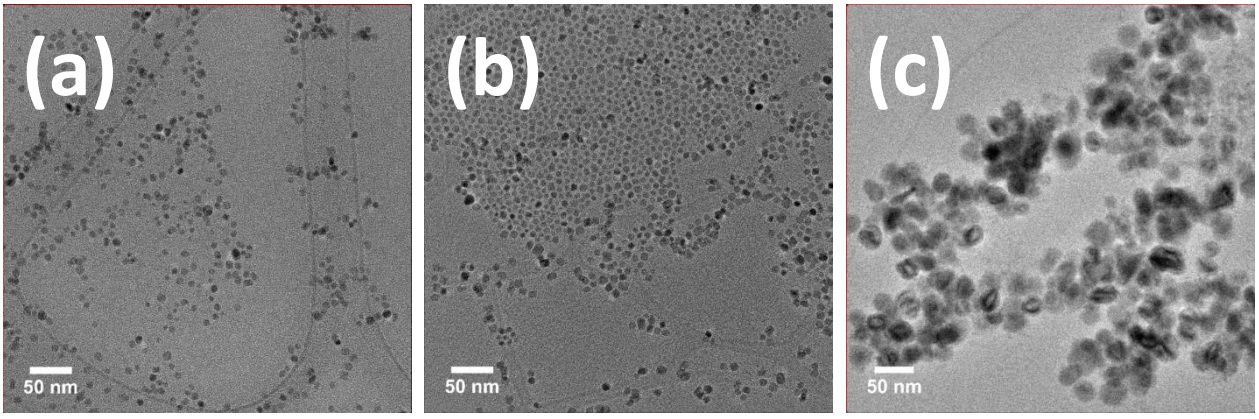

Fig. 7 TEM micrographs of **(a)** 39.9 kDa, **(b)** 40.2kDa, **(c)** 138.4 kDa PMMA-grafted nanoparticles in HMIM-TFSI.

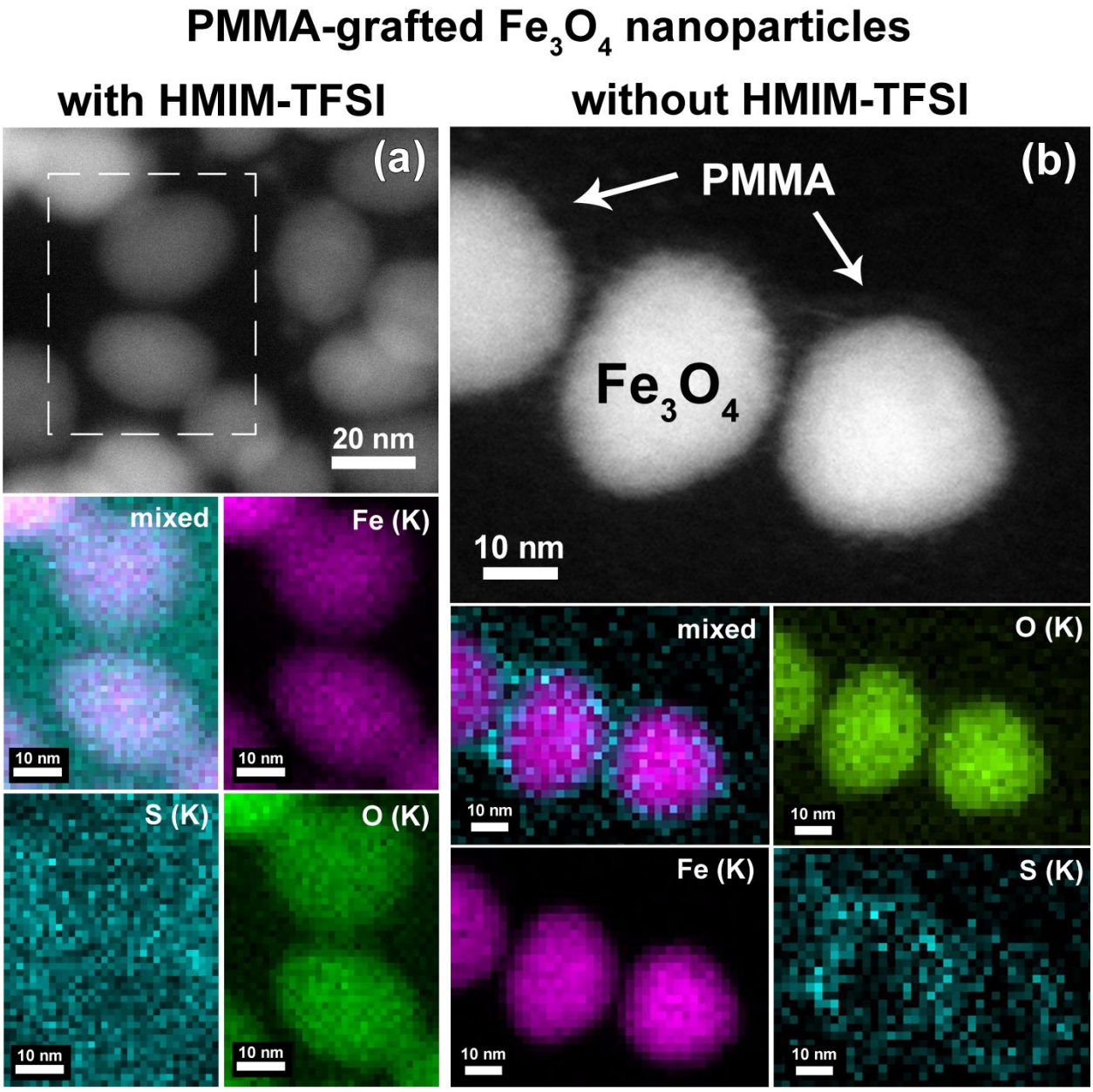

Fig. 8 ADF-STEM images and the corresponding EDX maps recorded using Fe, S, O Kα-signals as well as maps with overlapped (mixed) of these signals obtained from PMMA-grafted Fe_3O_4 nanoparticles **(a)** with HMIM-TFSI and **(b)** without HMIM-TFSI.

For the BMIM-BH_3 based systems with d-PMMA-grafted particles, both fast and slow diffusivities are close to that of the neat zwitterionic liquid indicating that the local mobility of BMIM-BH_3 is unaffected by particle dispersions (Fig. 6). TEM micrographs of particles in BMIM-BH_3 show strongly aggregated

structures with 40.2 kDa and 138.4 kDa samples (Fig. 9b-c). Even with relatively dispersed particles with an averaged particle-particle distance around 2.8 nm (Fig. 9a), the long-range translational diffusivity of BMIM-BH_3 is only slightly higher than in the neat ionic liquid. These results suggest that BMIM-BH_3 freely diffuses as in vehicular mechanism without interacting with polymers. The enhanced diffusivity of $HMIM^+$ is related to cation hopping as a result of $TFSI^-$ coupling with PMMA.

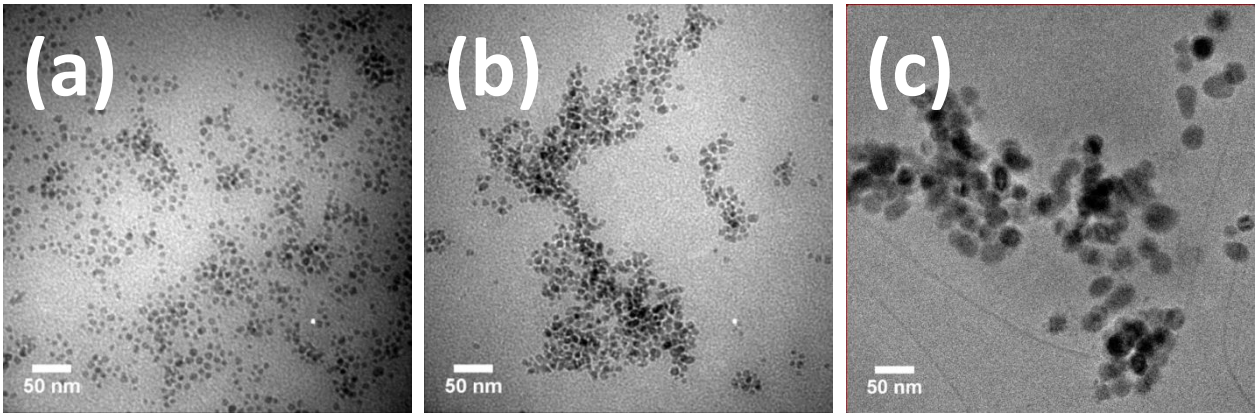

Fig. 9 TEM micrographs of **(a)** 39.9 kDa, **(b)** 40.2 kDa, **(c)** 138.4 kDa PMMA-grafted nanoparticles in BMIM-BH_3.

4. Conclusion

This work uniquely focuses on understanding the dynamics of HMIM-TFSI in the presence of PMMA-grafted nanoparticles. We demonstrated that PMMA coupling with HMIM-TFSI enhances the long-range $HMIM^+$ cation dynamics. Moreover, the long-range cation diffusion was significantly lower in close-packed particles compared to well-dispersed particles, and the confinement of HMIM-TFSI within these aggregated particles dominated the fast process, giving the highest constrained diffusion (~$60x10^{-10}$ m^2/s) in HMIM-TFSI. To further understand the polymer coupling effect, dynamics of zwitterionic liquid, BMIM-BH_3, was investigated in the presence of the same grafted particles. We found that diffusion processes of BMIM-BH_3 were not influenced with particle addition or dispersions. The cation diffusion

mechanism within the grafted particle structures substantiates the confinement and polymer coupling phenomenon that are essential for achieving high conductivity with grafted-particle based electrolytes. Works on relating the diffusion and conductivity in ion-containing copolymer grafted particles are currently being carried out to understand the proton transport mechanism in these model ionic liquid systems.

Acknowledgements

This work was supported by the National Science Foundation DMR Polymer program under award #1807802. Neutron scattering experiments were conducted at the Oak Ridge National Laboratory's Spallation Neutron Source with support from the Scientific User Facilities Division, Office of Basic Energy Science, U.S. Department of Energy (DOE). We thank Jessica Brandt and Steffen Tröger-Müller for help with the synthesis of the zwitterionic liquid.

References

1. B. Dyatkin, N. C. Osti, A. Gallegos, Y. Zhang, E. Mamontov, P. T. Cummings, J. Wu and Y. Gogotsi, *Electrochim. Acta*, 2018, **283**, 882-893.
2. R. Lin, P. Huang, J. Ségalini, C. Largeot, P. L. Taberna, J. Chmiola, Y. Gogotsi and P. Simon, *Electrochim. Acta*, 2009, **54**, 7025-7032.
3. C. Largeot, C. Portet, J. Chmiola, P.-L. Taberna, Y. Gogotsi and P. Simon, *J. Am. Chem. Soc.*, 2008, **130**, 2730-2731.
4. J. F. Brennecke and B. E. Gurkan, *J. Phys. Chem. Lett.*, 2010, **1**, 3459-3464.
5. W. Shi and D. R. Luebke, *Langmuir*, 2013, **29**, 5563-5572.
6. K. N. Ruckart, R. A. O'Brien, S. M. Woodard, K. N. West and T. G. Glover, *J. Phys. Chem. C*, 2015, **119**, 20681-20697.
7. J. N. A. Canongia Lopes and A. A. H. Pádua, *J. Phys. Chem. B*, 2006, **110**, 3330-3335.
8. B. Aoun, A. Goldbach, M. A. González, S. Kohara, D. L. Price and M.-L. Saboungi, *J. Chem. Phys.*, 2011, **134**, 104509.
9. W. Jiang, Y. Wang and G. A. Voth, *J. Phys. Chem. B*, 2007, **111**, 4812-4818.

10. M. Kofu, M. Nagao, T. Ueki, Y. Kitazawa, Y. Nakamura, S. Sawamura, M. Watanabe and O. Yamamuro, *J. Phys. Chem. B*, 2013, **117**, 2773-2781.
11. A. Triolo, O. Russina, H.-J. Bleif and E. Di Cola, *J. Phys. Chem. B*, 2007, **111**, 4641-4644.
12. M. Kofu, T. Someya, S. Tatsumi, K. Ueno, T. Ueki, M. Watanabe, T. Matsunaga, M. Shibayama, V. G. Sakai, M. Tyagi and O. Yamamuro, *Soft Matter*, 2012, **8**, 7888-7897.
13. F. Ferdeghini, Q. Berrod, J.-M. Zanotti, P. Judeinstein, V. G. Sakai, O. Czakkel, P. Fouquet and D. Constantin, *Nanoscale*, 2017, **9**, 1901-1908.
14. S. M. Chathoth, E. Mamontov, P. F. Fulvio, X. Wang, G. A. Baker, S. Dai and D. J. Wesolowski, *Europhys. Lett.*, 2013, **102**, 16004.
15. S. M. Chathoth, E. Mamontov, S. Dai, X. Wang, P. F. Fulvio and D. J. Wesolowski, *Europhys. Lett.*, 2012, **97**, 66004.
16. C. V. Cerclier, J.-M. Zanotti and J. L. Bideau, *Phys. Chem. Chem. Phys.*, 2015, **17**, 29707-29713.
17. J.-M. Z. Carole Cerclier, Jan Embs, and Jean Le Bideau *ECS Trans.*, 2014, 27-31.
18. Y. Liu, Y. Wang and J. Li, *Ionics*, 2016, **22**, 1681-1686.
19. S. Zhang, J. Zhang, Y. Zhang and Y. Deng, *Chem. Rev.*, 2017, **117**, 6755-6833.
20. R. Yan, M. Antonietti and M. Oschatz, *Adv. Energy Mater.*, 2018, **8**, 1800026.
21. N. C. Osti, K. L. Van Aken, M. W. Thompson, F. Tiet, D.-e. Jiang, P. T. Cummings, Y. Gogotsi and E. Mamontov, *J. Phys. Chem. Lett.*, 2017, 167-171.
22. M. P. Scott, M. Rahman and C. S. Brazel, *Eur. Polym. J.*, 2003, **39**, 1947-1953.
23. M. P. Scott, C. S. Brazel, M. G. Benton, J. W. Mays, J. D. Holbrey and R. D. Rogers, *Chem. Commun.*, 2002, 1370-1371.
24. M. A. B. H. Susan, T. Kaneko, A. Noda and M. Watanabe, *J. Am. Chem. Soc.*, 2005, **127**, 4976-4983.
25. S. Tröger-Müller, M. Antonietti and C. Liedel, *Phys. Chem. Chem. Phys.*, 2018, **20**, 11437-11443.
26. S. Tröger-Müller and C. Liedel, *Batteries & Supercaps*, 2019, **2**, 223-228.
27. J. Park, K. An, Y. Hwang, J.-G. Park, H.-J. Noh, J.-Y. Kim, J.-H. Park, N.-M. Hwang and T. Hyeon, *Nat. Mater.*, 2004, **3**, 891-895.
28. S. Sun, H. Zeng, D. B. Robinson, S. Raoux, P. M. Rice, S. X. Wang and G. Li, *J. Am. Chem. Soc.*, 2004, **126**, 273-279.
29. C. Li, J. Han, C. Y. Ryu and B. C. Benicewicz, *Macromolecules*, 2006, **39**, 3175-3183.
30. Y. Jiao and P. Akcora, *Macromolecules*, 2012, **45**, 3463-3470.
31. E. Mamontov and K. W. Herwig, *Rev. Sci. Instrum.*, 2011, **82**, 085109.

32. O. Arnold, J. C. Bilheux, J. M. Borreguero, A. Buts, S. I. Campbell, L. Chapon, M. Doucet, N. Draper, R. Ferraz Leal, M. A. Gigg, V. E. Lynch, A. Markvardsen, D. J. Mikkelson, R. L. Mikkelson, R. Miller, K. Palmen, P. Parker, G. Passos, T. G. Perring, P. F. Peterson, S. Ren, M. A. Reuter, A. T. Savici, J. W. Taylor, R. J. Taylor, R. Tolchenov, W. Zhou and J. Zikovsky, *Nucl. Instrum. Methods Phys. Res., Sect. A*, 2014, **764**, 156-166.
33. R. T. Azuah, L. R. Kneller, Y. Qiu, P. L. W. Tregenna-Piggott, C. M. Brown, J. R. D. Copley and R. M. Dimeo, *J. Res. Natl. Inst. Stand. Technol.*, 2009, **114**, 341-358.
34. T. Burankova, E. Reichert, V. Fossog, R. Hempelmann and J. P. Embs, *J. Mol. Liq.*, 2014, **192**, 199-207.
35. E. Mamontov, H. Luo and S. Dai, *J. Phys. Chem. B*, 2009, **113**, 159-169.
36. J. M. Crosthwaite, M. J. Muldoon, J. K. Dixon, J. L. Anderson and J. F. Brennecke, *J. Chem. Thermodyn.*, 2005, **37**, 559-568.
37. Y. Shimizu, Y. Ohte, Y. Yamamura, K. Saito and T. Atake, *J. Phys. Chem. B*, 2006, **110**, 13970-13975.
38. C. J. Jafta, C. Bridges, L. Haupt, C. Do, P. Sippel, M. J. Cochran, S. Krohns, M. Ohl, A. Loidl, E. Mamontov, P. Lunkenheimer, S. Dai and X.-G. Sun, *ChemSusChem*, 2018, **11**, 3512-3523.
39. B. Aoun, M. A. González, J. Ollivier, M. Russina, Z. Izaola, D. L. Price and M. L. Saboungi, *J. Phys. Chem. Lett.*, 2010, **1**, 2503-2507.
40. P. G. De Gennes, *Physica*, 1959, **25**, 825-839.
41. E. Mamontov, G. A. Baker, H. Luo and S. Dai, *Chem.Phys.Chem.*, 2011, **12**, 944-950.
42. M. L. Hoarfrost, M. Tyagi, R. A. Segalman and J. A. Reimer, *J. Phys. Chem. B*, 2012, **116**, 8201-8209.

in HMIM-TFSI

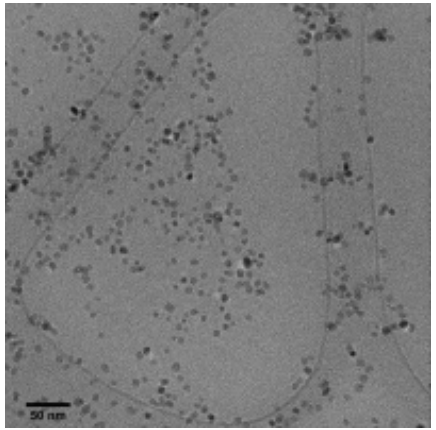

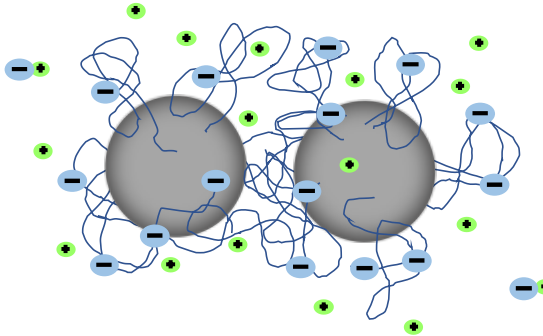

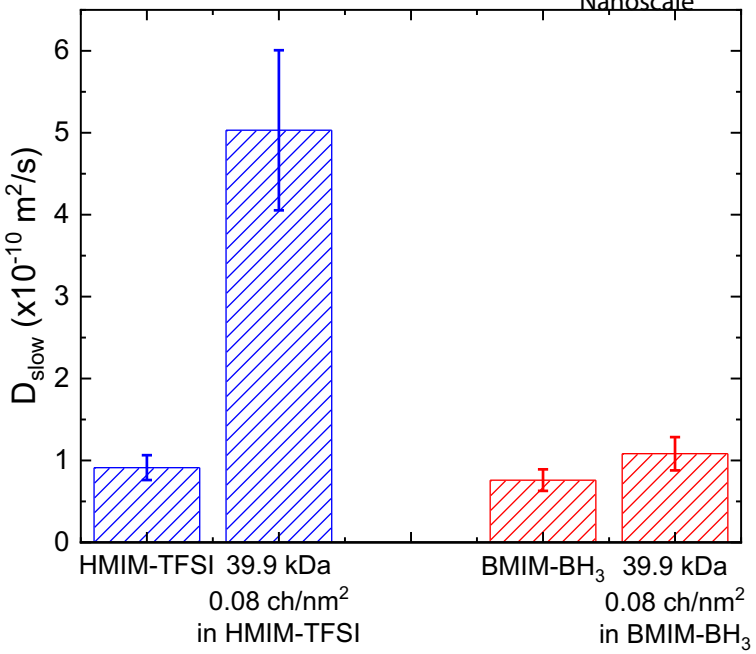

in BMIM-BH_3

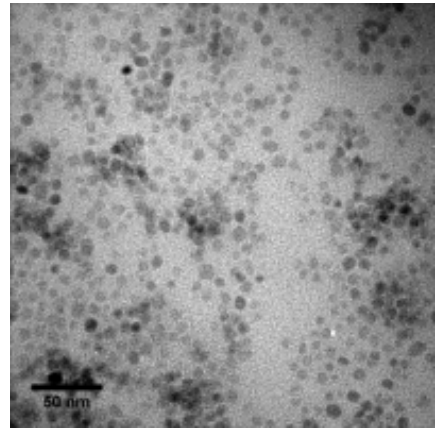

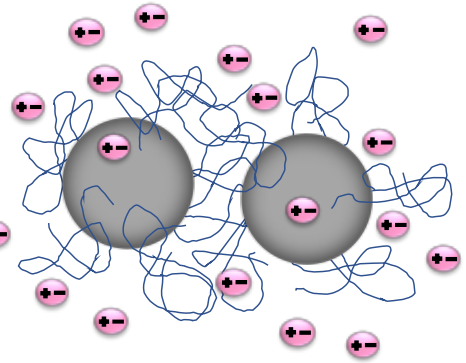

= cation (HMIM)

= anion (TFSI)

= BMIM-BH_3

Long-range diffusion coefficient (D_{slow}) of $HMIM^+$ cations is higher than that of zwitterionic liquid (BMIM-BH_3) when mixed with the polymer.